Evidence of magnetic flux ropes downstream of the heliospheric termination shock

Journal of Physics: Conference Series **1620** (2020) 012027 doi:10.1088/1742-6596/1620/1/012027

Evidence of magnetic flux ropes downstream of the heliospheric termination shock

L L Zhao[1], G P Zank[1,2], L Adhikari[1], Q Hu[1,2], J le Roux[1,2]

[1] Center for Space Plasma and Aeronomic Research (CSPAR), University of Alabama in Huntsville, Huntsville, AL 35899, USA

[2] Department of Space Science, University of Alabama in Huntsville, Huntsville, AL 35899, USA

E-mail: lz0009@uah.edu

Abstract. *Voyager* 1 and 2 observed enhanced energetic particle fluxes downstream of the heliospheric termination shock. In this paper, we provide observational evidence of reconnection processes downstream of the shock by applying a wavelet analysis technique to three magnetohydrodynamics (MHD) invariants from the magnetic field and plasma fluctuations in the post-HTS region measured by *Voyager* 2. Our results suggest the existence of possible magnetic islands/flux ropes structures within ∼1 AU behind the HTS. The location and scales of these structures are characterized by wavelet spectrograms of the normalized reduced magnetic helicity, normalized cross helicity, and normalized residual energy. Transport theory suggests that these structures may contribute to the acceleration of energetic particles through magnetic reconnection processes. We use a kinetic transport theory to model the energetic proton flux in the region downstream of the HTS. Our results suggest that stochastic acceleration due to magnetic reconnection can explain the ACR proton flux enhancement at a short distance beyond the HTS.

1. Introduction

A curious observation made by *Voyagers* [4, 5, 1, 13] is that the anomalous cosmic ray (ACR) intensity peaks at a short distance (within ∼1 au) downstream of the heliospheric termination shock (HTS), contradicting the classic diffusive shock acceleration (DSA) theory. A possible explanation is that enhanced magnetic reconnection and the subsequent production of small-scale magnetic flux ropes in the heliosheath immediately downstream of the HTS occurs as a result of the interaction of the wavy heliospheric current sheet with the HTS [14, 2, 3, 10, 11, 12]. To validate the theory, it is necessary to confirm whether magnetic islands/flux rope structures exist in the heliosheath, which remains unclear. In this paper, we provide evidence of the presence of magnetic islands downstream of the HTS and the simultaneous local acceleration of particles due to magnetic reconnection processes. The full results were reported in a previous publication [8].

Magnetic island or flux rope structures have been observed throughout the heliosphere [7, 8, 18, 6]. The simplest method to identify these structures is to look for rotation of the magnetic field [15]. Recently, more advanced techniques have been developed to make the identification more efficient. One technique is the Grad-Shafranov reconstruction method, based on an automatic detection scheme for small-scale magnetic flux ropes [16, 17]. Another method

is to use magnetic helicity as a proxy since it indicates the rotation of magnetic field. Strictly speaking, the magnetic helicity, $H = \int \mathbf{A} \cdot \mathbf{B} dV$ where $\mathbf{A}$ is the vector potential and $\mathbf{B}$ is the magnetic field strength [19, 20, 21], cannot be obtained from single spacecraft measurements as it depends on the three dimensional magnetic field topology. However, a reduced form of magnetic helicity can be estimated even with a single spacecraft based on spectral analysis [19]. Magnetic flux ropes can be identified as structures with enhanced magnetic helicity as they possess helical magnetic field lines. By using a wavelet analysis, the time evolution of the reduced magnetic helicity can be studied [21], and observations at 1 au confirm a good correspondence between magnetic flux ropes and high magnetic helicity. Caution should be exercised regarding Alfvénic structures, which can exhibit similar signatures as magnetic flux ropes. These two types of structures may be distinguished from each other by spectra of cross helicity and residual energy [24, 22]. Ref [26] compared the wavelet and Fourier transform methods in calculating the magnetic power spectrum and the reduced magnetic helicity, using *Wind* 92 seconds magnetic field measurements. The two methods are found to be consistent with each other.

In the following sections, we present our technique to identify magnetic islands/flux ropes and the application to the *Voyager* 2 magnetic field and plasma observations near the HTS crossing. We show spectrograms of the reduced normalized magnetic helicity, cross helicity, and residual energy based on a Morlet wavelet analysis. We also quantitatively compare the observed ACR proton "time-intensity" profiles immediately downstream of the HTS with a transport model of reconnection acceleration.

2. Identification of magnetic islands

Magnetic flux ropes or islands are expected to have a high value of magnetic helicity, corresponding to the structure of helical magnetic field lines. A statistical study of magnetic flux ropes at 1 au was carried out in Ref [21], and they found that the structures are in high magnetic helicity states. Following the method of Ref [20], we use a Morlet wavelet analysis and apply it to magnetic helicity, cross helicity, and residual energy. The three turbulence quantities can be calculated by the Elsässer variables,

$$\mathbf{z}^{\pm} = \mathbf{u} \pm \frac{\mathbf{b}}{\sqrt{4\pi n_p m_p}}, \tag{1}$$

where $\mathbf{u}$ and $\mathbf{b}$ represent the fluctuating velocity and magnetic field, n_p is the proton number density, and m_p is the proton mass. Fluctuating magnetic and velocity fields are separated from the mean fields as $\underline{\mathbf{B}} = \mathbf{B}_0 + \mathbf{b}$; $\underline{\mathbf{U}} = \mathbf{U}_0 + \mathbf{u}$. Here, $\mathbf{B}_0$ is the mean magnetic field, $\mathbf{U}_0$ the mean velocity field, and the conditions $\langle \underline{\mathbf{B}} \rangle = \mathbf{B}_0$ and $\langle \mathbf{b} \rangle = 0$ (similar for the velocity) are satisfied. The Elsässer variables $\mathbf{z}^+$ ($\mathbf{z}^-$) represents the forward (backward) propagating modes with respect to the mean magnetic field orientation. After performing the Wavelet transforms [27] on three fluctuating magnetic field components b_R, b_T, b_N, the normalized reduced magnetic helicity can be estimated by [19, 21, 26]

$$\sigma_m(\nu, t) = \frac{2\,\mathrm{Im}[W_T^*(\nu, t) \cdot W_N(\nu, t)]}{|W_R(\nu, t)|^2 + |W_T(\nu, t)|^2 + |W_N(\nu, t)|^2}, \tag{2}$$

where ν is the wavelet frequency (related to the data resolution). The symbols $W_R(\nu, t)$, $W_T(\nu, t)$ and $W_N(\nu, t)$ are the wavelet transforms of the magnetic field components b_R, b_T and b_N. The conjugate of $W_T(\nu, t)$ is denoted by $W_T^*(\nu, t)$. The spectrogram of the magnetic helicity σ_m, allows one to determine both the magnitude and the handedness of underlying fluctuations at a specific scale. A positive value of σ_m corresponds to righ-handed chirality and a negative value to left-handed chirality.

The complex Morlet wavelet function $\psi(t') = \frac{1}{\pi A} \exp^{-\frac{t'^2}{A}} \exp^{i2\pi C t'}$ with bandwidth $A = 1.0$ and cent

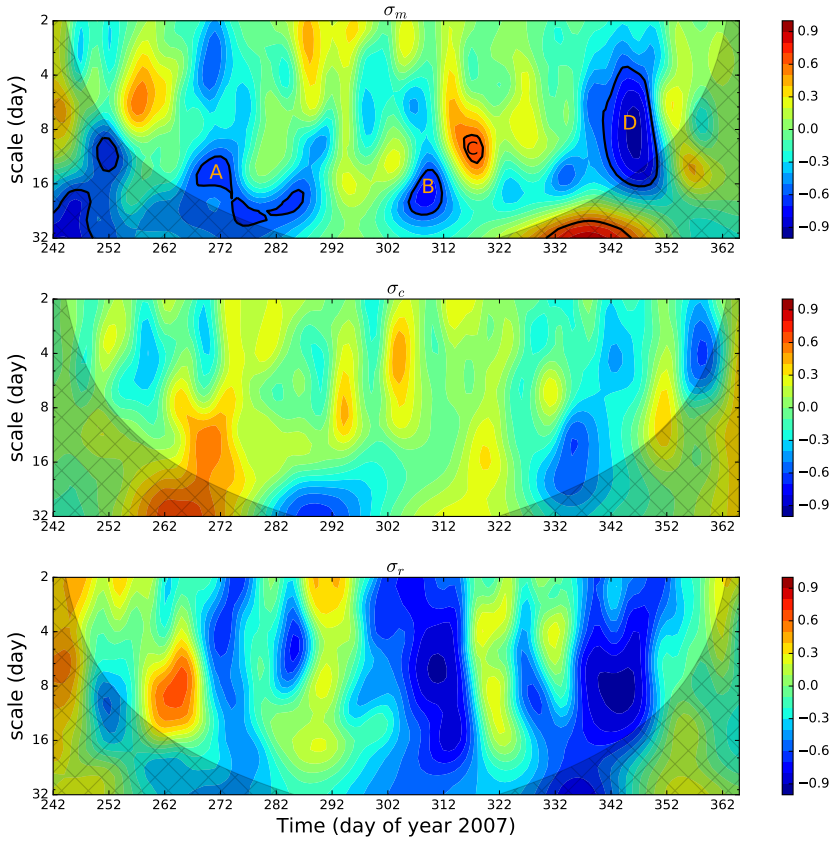

Figure 1. The wavelet spectrograms of three turbulence quantities during a 124-day period behind the heliospheric termination shock. The top panel plots the normalized reduced magnetic helicity σ_m. The middle panel plots the normalized cross helicity σ_c. The bottom panel plots the normalized residual energy σ_r. The cone of influence (COI) due to edge effects is indicated by the shaded cross areas in the figure.

According to Ref [23], the normalized cross helicity σ_c and normalized residual energy σ_r can be evaluated by the Elsässer variables $\mathbf{z}^{\pm}$ as

$$\sigma_c = \frac{\langle z^{+2} \rangle - \langle z^{-2} \rangle}{\langle z^{+2} \rangle + \langle z^{-2} \rangle}, \tag{3}$$

and

$$\sigma_r = \frac{2\langle \mathbf{z}^{+} \cdot \mathbf{z}^{-} \rangle}{\langle z^{+2} \rangle + \langle z^{-2} \rangle}, \tag{4}$$

where $\langle z^{+2} \rangle$ ($\langle z^{-2} \rangle$) represents the energy density in forward (backward) propagating modes. The normalization ensures that the absolute values of σ_m, σ_c and σ_r do not exceed unity. Physically, the normalized cross helicity σ_c corresponds to the alignment between magnetic and velocity fluctuations. Ideally, a single Alfvén wave has a large cross helicity ($|\sigma_c| \simeq 1$). On the other hand, the normalized residual energy σ_r represents the difference between the fluctuating kinetic energy and magnetic energy. Dominant magnetic fluctuating energy leads to a negative

residual energy ($\sigma_r < 0$), and vice versa for cases where kinetic fluctuating energy dominates. After applying the wavelet transform $\mathcal{W}$ to the Elsässer components $z_R^{\pm}$, $z_T^{\pm}$, and $z_N^{\pm}$, we obtain spectrograms in σ_r and σ_c as

$$\sigma_r(\nu,t) = \frac{2\,\mathrm{Re}[\mathcal{W}^*(z_R^+)\cdot\mathcal{W}(z_R^-) + \mathcal{W}^*(z_T^+)\cdot\mathcal{W}(z_T^-) + \mathcal{W}^*(z_N^+)\cdot\mathcal{W}(z_N^-)]}{W^+(\nu,t) + W^-(\nu,t)}, \tag{5}$$

and

$$\sigma_c(\nu,t) = \frac{W^+(\nu,t) - W^-(\nu,t)}{W^+(\nu,t) + W^-(\nu,t)}, \tag{6}$$

where $W^+(\nu,t)$ and $W^-(\nu,t)$ represents the wavelet power spectrum in $\mathbf{z}^+$ and $\mathbf{z}^-$ modes, respectively. Thus, $W^+(\nu,t) = |\mathcal{W}(z_R^+)|^2 + |\mathcal{W}(z_T^+)|^2 + |\mathcal{W}(z_N^+)|^2$ and $W^-(\nu,t) = |\mathcal{W}(z_R^-)|^2 + |\mathcal{W}(z_T^-)|^2 + |\mathcal{W}(z_N^-)|^2$.

The spectrograms of σ_m, σ_c, and σ_r defined above are illustrated in Figure 1. Daily averaged magnetic field and plasma data measured by *Voyager* 2 between 2007 August 30 (Day 242 of 2007) to 2007 December 31 (Day 365 of 2007) are used. We choose a set of scales between 2 days and 32 days for the wavelet analysis, corresponding to the scale sizes of the structures identifiable by the method. The cone of influence (COI) is plotted as shaded cross areas in the figure. Results in these regions may not be reliable due to edge effects. Several possible magnetic flux rope structures are readily seen from Figure 1, and identified by the letters A, B, C, and D. The boundaries of these structures are chosen at $|\sigma_m| = 0.6$. Table 1 lists the parameters of these four structures, including their mean magnetic helicity σ_m, cross helicity σ_c, and residual energy σ_r. The central time and scale in the table are determined by the peak of σ_m in time and scale. As shown in Table 1, all four of the identified structures are associated with a small cross helicity $|\sigma_c| < 0.3$ and negative residual energy, which indicates that they are more likely to be magnetic flux ropes than Alfvénic stuctures. Especially in structures B and D, both of which have highly negative residual energy, indicating magnetic flux ropes rather than fluid vortices. We can also determine that structures A, B, and D have a left-hand chirality, while structure C has a right-hand chirality.

Table 1. List of magnetic flux ropes identified in the spectrograms.

No.	Central time (UT)	Scale (day)	Magnetic helicity σ_m	Cross helicity σ_c	Residual energy σ_r
A	2007/10/03	17	-0.63	0.27	-0.23
B	2007/11/05	18	-0.69	-0.04	-0.66
C	2007/11/14	10	0.65	0.14	-0.36
D	2007/12/12	8	-0.77	-0.15	-0.78

The magnetic power spectral density (PSD) can be calculated as a function of frequency from the wavelet spectrogram by averaging over time. The results are plotted in Figure 2, where the PSD upstream (2007 May 1 to 2007 August 30) and downstream (2007 August 30 to 2007 December 31) of the shock are plotted as red and green curves. Both intervals contain ∼120 days of data. It can be clearly seen from the figure that the power in magnetic fluctuations is higher downstream than upstream. This indicates that the HTS may amplify turbulent fluctuations and may generate structures such as small-scale magnetic flux ropes. Both upstream and downstream spectra are consistent with a Kolmogorov $k^{-5/3}$ power law over certain frequency range, as demonstrated by the black dashed line. Because the termination shock is quasi-perpendicular, there is no apparent upstream wave activity [25]. The magnetic PSD of Figure 2 provides further evidence supporting the dominance of quasi-2D structures downstream of the HTS, consistent with Figure 1.

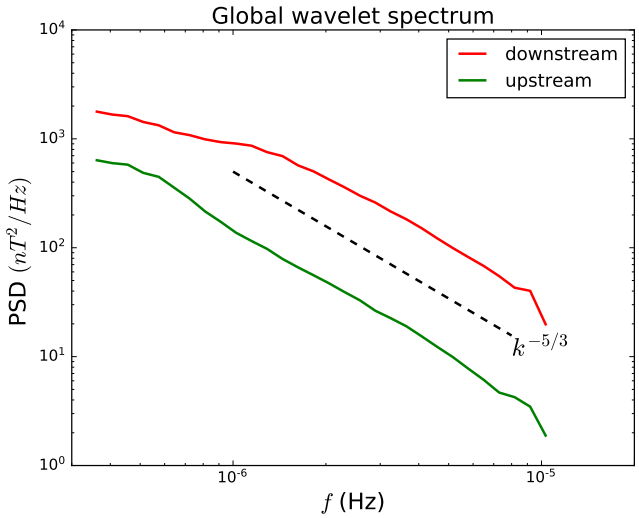

Figure 2. The red and green curves plot the averaged magnetic power spectral density calculated from wavelet analysis upstream and downstream of the shock. A $k^{-5/3}$ spectrum is displayed as a reference.

3. Modeling the observed ACR fluxes

Following Ref [7], we apply the analytic formula from a statistical particle acceleration theory [2] to explain the enhanced ACR proton intensities measured by *Voyager* 2 in nine energy channels: 1.8–2.2 MeV, 2.2–3.0 MeV, 3.0–4.6 MeV, 4.6–6.2 MeV, 6.2–7.7 MeV, 7.7–10.3 MeV, 10.3–12.8 MeV, 12.8–15.3 MeV, and 15.3-17.9 MeV. The average energies of the corresponding channels are 2.0 MeV, 2.6 MeV, 3.8 MeV, 5.4 MeV, 6.95 MeV, 9.0 MeV, 11.55 MeV, 14.05 MeV, and 16.6 MeV. The theoretical model takes into account two basic acceleration mechanisms for ACR protons: first-order Fermi acceleration due to contracting magnetic field lines, and direct acceleration due to the reconnection electric field generated by island merging. After a series of simplifying assumptions, the analytic solution for the particle distribution function can be derived [2]. Ref [7] further incorporates an escape term into the analytic solution. Specifically, the acceleration model is parameterized by (i) the strength of the reconnection electric field V_E (with the dimension of velocity), (ii) the dimensionless particle escape rate τ_d/τ_e, and (iii) the dimensionless island contraction rate τ_d/τ_c. The escape rate and the contraction rate are both normalized by the diffusion time scale τ_d. Three additional parameters j_0, E_0, L_{diff} are used for normalization in the model. To derive the analytical solution, all these parameters are assumed to be constants in space and time, and are energy independent.

In previous work [7, 6], a simple trial-and-error approach was adopted to obtain a qualitative fit. To obtain more quantitative results and to quantify uncertainties, we employ a Monte Carlo Markov Chain (MCMC) technique to find a set of best-fit model parameters. The MCMC is a powerful technique for fitting data to a parameterized model when a simple formula (such as linear regression) does not exist, with the added benefit of obtaining the associated confidence interval for each parameter. The basic idea of MCMC is to search for parameters that maximize the likelihood of the model given some experimental data. At each step of the chain, a new set of parameters called candidates are drawn randomly from a proposed distribution. The candidates are accepted if the likelihood is larger than that of the previous step. When the likelihood is smaller than the previous step, the candidates are accepted in a Monte Carlo fashion according to the Metropolis-Hastings algorithm, which avoids trapping in a local maximum. After a sufficient number of iterations, the median of all accepted values are taken as best-fit parameters. The

confidence interval at a certain level can be approximated as the corresponding quantiles of the chain.

In principle, the model parameters need to be independent of one another for MCMC to work properly, which may not be easily justified. In our case, there are six parameters in the model, three of which are fixed and used for normalization. These include the particle diffusion length $L_{diff} = 8.0 \times 10^{12}$ cm, the particle injection energy $E_0 = 0.2$ MeV, and the particle flux at the injection point $j_0 = 7.0 \times 10^3$ cm^{-2}s^{-1}sr^{-1} MeV^{-1}. The remaining three parameters V_E, τ_d/τ_c, and τ_d/τ_e, are free parameters to be iterated in MCMC. We choose a point ~ 22 days behind the shock as the injection point (on 2007/09/22) where low-energy particle fluxes are near a local minimum. For each set of parameters, we calculate the model predictions of the particle flux at all the times and energies that we consider. Each measurement is assumed to be distributed like a Gaussian random variable, so that the likelihood of the model can be estimated by the chi-square: $\chi^2 = \sum_i (y_i - \hat{y}_i)^2/\sigma_i^2$, where y_i is the observed particle intensity, σ_i is the uncertainty or standard deviation of the observation, and $\hat{y}_i$ is the model predicted flux. After applying MCMC, we find the following 68% confidence intervals (1-σ) for the three free parameters,

$$V_E/U \in [0.055, 0.058]; \qquad \tau_d/\tau_c \in [0.161, 0.173]; \qquad \tau_d/\tau_e \in [6.165, 6.267]. \tag{7}$$

A constant solar wind velocity of $U = 140$ km/s has been assumed in the inner heliosheath. The best-fit parameters are obtained as the median values,

$$V_E/U = 0.056; \qquad \tau_d/\tau_c = 0.167; \qquad \tau_d/\tau_e = 6.219. \tag{8}$$

We now discuss briefly the physical implications of the best-fit parameters. First, $\tau_d < \tau_c$ suggests that the particle diffusion time scale is smaller than the island contraction time scale, meaning that particles may be energized diffusively in the region containing multiple magnetic islands. This is because particles have sufficient time to diffuse between multiple islands during the time when a flux rope experiences significant contraction. Correspondingly, the relation $\tau_e < \tau_d$ suggests that the particle escape process is efficient compared to particle diffusion. This is crucial for the relatively soft energy spectrum for events observed in the inner heliosphere [6]. We note that the reduced chi-square value of the model is around 55 with the best-fit parameters, contradicting the idealized situation where the reduced chi-square should be about unity. In our case, the reduced chi-square value is significantly larger than what is expected for a model that is consistent with the data. An explanation is that our model is not intended to explain fine-scale fluctuations in the energetic particle fluxes. In other words, there are intrinsic fluctuations that have not been taken into account by the model. It should also be pointed out that the fixed parameters L_{diff}, E_0 and j_0 are chosen somewhat arbitrarily. The value of parameter L_{diff} may be justified by its definition $L_{diff} = \kappa/U$, where κ is the diffusion coefficient for particles, and U is the solar wind speed. Thus our choice of L_{diff} translates to a diffusion coefficient of $\kappa = 1.12 \times 10^{20}$ cm^2/s assuming a solar wind speed of $U = 140$ km/s. The diffusion coefficient is also related to the mean free path (mfp) by $\kappa = \lambda v/3$, where λ is the mfp and v is the particle velocity. If we use 3.66×10^7 m/s as a representative velocity in our considered energy range (corresponding to ~ 7 MeV), we find an mfp of $\lambda = 3\kappa/v = 0.9 \times 10^9$ m~ 0.006 au. Some other parameters follow as the diffusion time scale being $\tau_d = L_{diff}/U = 5.7 \times 10^5$ s; the island contraction time scale being $\tau_c = \tau_d/(\tau_d/\tau_c) = 3.4 \times 10^6$ s; and the escape time scale being $\tau_e = \tau_d/(\tau_d/\tau_e) = 9.1 \times 10^4$ s. The electric field parameter is $M_E = (V_E/U)^{-1} \simeq 18$. Since we consider an injection energy (0.2 MeV) far below the considered energy range, there are no data to justify the choice of parameter j_0 directly. Nevertheless, the model does agree reasonably well with the observations, at least qualitatively. Figure 3 illustrates a comparison between the model particle flux with best-fit parameters and the observed data with uncertainties.

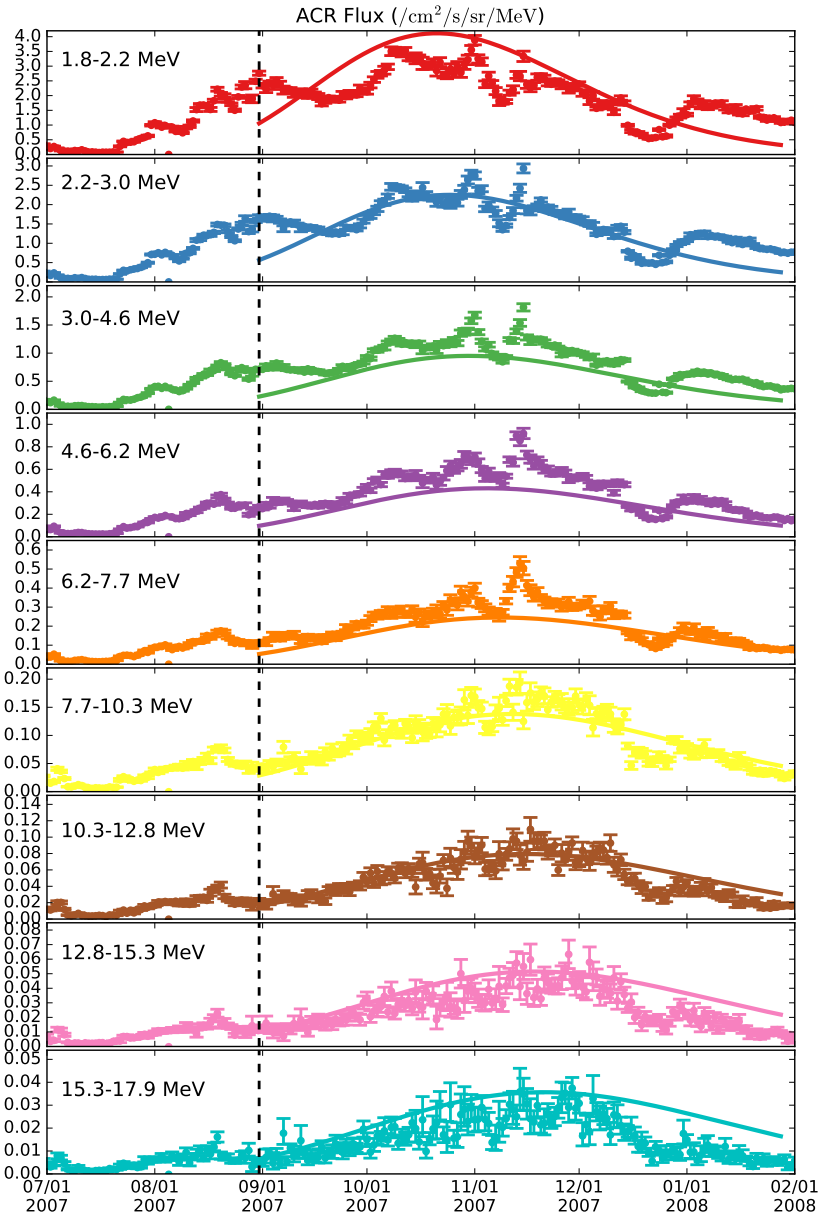

Figure 3. Scatter plots of ACR proton fluxes observed by *Voyager* 2 between 2007 July 1 and 2008 February 1. The uncertainties are plotted as error bars. The solid curves show our modeling results with the best-fit parameters. The dashed vertical line represents the HTS crossing.

The ACR proton flux observed by *Voyager* 2 is reasonably well-fitted by the model especially for high energy channels. Figure 3 displays the time-intensity profile of the ACR proton flux in nine energy channels in the range 1.8–17.9 MeV. We average the data to a one-day resolution for the selected period from 2007 July 1 to 2008 February 1. The uncertainties of the observed proton flux are calculated from the observed counts N (assuming a Poisson distribution). The HTS crossing by *Voyager* 2 is identified as the vertical dashed line in the figure. The curves of different colors behind the HTS are modeling results with the best-fit parameters that have been obtained from MCMC. It is clear from the figure that our model does not fit very well with the

lower energy channels, but appears to be fairly consistent with the higher energy bands within uncertainties. The model does reproduce some general features of the observational data. For each energy channel, the downstream proton intensity is amplified relative to the value at the shock. The peak amplification is about ~ 2 times for the 1.8–2.2 MeV energy channel and ~ 4 times for the 15.3–17.9 MeV energy channel. This is roughly consistent with the model which predicts that the flux amplification factor is ordered in ascending order with increasing energy. The distance between the peak of the energetic particle flux and the HTS also increases with increasing particle energy. High-energy particles (> 4.6 MeV) fluxes are observed to peak more than 2 months after the HTS crossing. This is also reproduced by the model [2, 3, 7].

We emphasize again that there are numerous simplifying assumptions in building the model. These include a 1D geometry with a constant solar wind velocity; constant and energy-independent acceleration parameters such as the contraction rate and reconnection electric field; nearly isotropic particle distributions, and negligible second-order Fermi acceleration, etc. Naturally, one should not expect such a simple model to fit perfectly with the observational data, as is made clear by the very large reduced chi-square (about 55). There are also small-scale fluctuations and inhomogeneities in the solar wind that will likely contribute to the deviation between the model and observed particle fluxes, and we certainly do not exclude other possible mechanisms that may accelerate ACRs.

4. Summary

In this paper, we briefly report evidence of magnetic flux rope structures in the inner heliosheath region downstream of the HTS. The complete analysis has been reported in Ref [8]. Observational evidence for magnetic islands downstream of the HTS is found using a wavelet analysis of several turbulence quantities including the normalized reduced magnetic helicity, cross-helicity, and residual energy. The magnetic field and plasma data measured by *Voyager* 2 are used in this study. Using Morlet wavelet spectrograms, we determined the location and scales of several magnetic flux rope structures in the inner heliosheath. Previous studies ranging from 1 to 5 au found multiple small-scale magnetic flux ropes [16, 17] in the solar wind. Obviously, the number of flux ropes which can be identified in this study is very limited compared to numerical simulations such as Ref [14] because of the poor data resolution available. Nevertheless, there is evidence for the existence of possible magnetic flux rope structures in the region downstream of the HTS.

Following our previous work [7], the observed energetic proton flux in the region downstream of the HTS is studied using a kinetic transport theory that includes acceleration mechanisms related to magnetic reconnection and magnetic island merging and contracting [2]. To improve the fitting procedure of Ref [7], we apply the MCMC technique to find the best-fit parameters of the model. Our results with the best-fit parameters agree reasonably well with the observed evolution of ACR proton flux downstream of the HTS. Our resultant proton flux indicates that the ACR proton flux observed by *Voyager* 2 within ~ 1 au behind the HTS is well explained by stochastic acceleration due to the interaction of magnetic islands.

Acknowledgments

We acknowledge the partial support of the NSF EPSCoR RII-Track-1 Cooperative Agreement OIA-1655280, an NSF-DOE grant PHY 1707247 and NASA grant/subaward 0000167 (NNX17ABO4G).

References

[1] Decker, R. B., Krimigis, S. M., Roelof, E. C., et al. 2005, *Science*, 309, 2020
[2] Zank, G. P., le Roux, J. A., Webb, G. M., et al. 2014, *ApJ*, 797, 28
[3] Zank, G. P., Hunana, P., Mostafavi, P., et al. 2015, *APJ*, 814, 137

[4] Stone, E. C., Cummings, A. C., & McDonald, F. B., et al. 2005, *Science*, 309, 2017
[5] Stone, E. C., Cummings, A. C., McDonald, F. B., et al. 2008, *Nature*, 45 4, 71
[6] Adhikari, L., Khabarova, O., Zank, G. P., & Zhao, L.-L. 2019, *ApJ*, 873, 72
[7] Zhao, L.-L., Zank, G. P., Khabarova, O., et al. 2018, *ApJ*, 864, L34
[8] Zhao, L.-L., Zank, G. P., Hu, Q., et al. 2019, *ApJ*, 886, 144
[9] Du, S., Guo, F., Zank, G. P., Li, X., & Stanier, A. 2018, *ApJ*, 867, 16
[10] le Roux, J. A., Zank, G. P., Webb, G. M., & Khabarova, O. 2015, *ApJ*, 801, 112
[11] le Roux, J. A., Zank, G. P., Webb, G. M., & Khabarova, O. V. 2016, *ApJ*, 827, 47
[12] le Roux, J. A., Zank, G. P., & Khabarova, O. V. 2018, *ApJ*, 864, 158
[13] Senanayake, U. K., Florinski, V., Cummings, A. C., et al. 2015, *ApJ*, 804, 12
[14] Drake, J. F., Opher, M., Swisdak, M., & Chamoun, J. 2010, *ApJ*, 709, 963
[15] Moldwin, M. B., Phillips, J. L., Gosling, J. T., et al. 1995, *J. Geophys. Res.*, 100, 19903
[16] Zheng, J., & Hu, Q. 2018, *ApJL*, 852, L23
[17] Hu, Q., Zheng, J., Chen, Y., le Roux, J., & Zhao, L. 2018, *ApJS*, 239, 12
[18] Zhao, L.-L., Zank, G. P., Adhikari, L., et al. 2020, *ApJS*, 246, 26
[19] Matthaeus, W. H., Goldstein, M. L., & Smith, C. 1982, *Physical Review Letters*, 48, 1256
[20] Telloni, D., Bruno, R., D'Amicis, R., et al. 2012, *ApJ*, 751, 19
[21] Telloni, D., Perri, S., Bruno, R., et al. 2013, *ApJ*, 776, 3
[22] Adhikari, L., Zank, G. P., Hunana, P., et al. 2017, *ApJ*, 841, 85
[23] Zank, G. P., Dosch, A., Hunana, P., et al. 2012, *ApJ*, 745, 35
[24] Zank, G. P., Adhikari, L., Hunana, P., et al. 2017, *ApJ*, 835, 147
[25] Zank, G. P., Li, G., Florinski, V., et al. 2006, *J. Geophys. Res.*, 111, A6
[26] Vasquez, B. J., Markovskii, S. A., & Smith, C. W. 2018, *ApJ*, 855, 121
[27] Torrence, C., & Compo, G. P. 1998, *Bulletin of the American Meteorological Society*, 79, 61